Numerical Study of the Flow Around a Bus-Shaped Body

Siniša Krajnović
e-mail: sinisa@tfd.chalmers.se

Lars Davidson

Department of Thermo and Fluid Dynamics,
Chalmers University of Technology,
SE-41296 Gothenburg, Sweden

Flow around a simplified bus is analyzed using large-eddy simulation. At the Reynolds number of 0.21×10^6, based on the model height and the incoming velocity, the flow produces features and aerodynamic forces relevant for the higher (interesting in engineering) Reynolds number. A detailed survey of both instantaneous and time-averaged flows is made and a comparison with previous knowledge on similar flows is presented. Besides the coherent structures observed in experimental and previous numerical studies, new smaller-scale structures were registered here. The mechanisms of formation of flow structures are explained and the difference between instantaneous and time-averaged flow features found in the experimental observations is confirmed. Aerodynamic forces are computed and their time history is used to reveal the characteristic frequencies of the flow motion around the body. A comparison is made of pressure and velocity results with experimental data and shows fairly good agreement. [DOI: 10.1115/1.1567305]

1 Introduction

The time-averaged flow around cars is fairly well known and understood, [1]. In contrast, the instantaneous flow has until recently been unstudied and still remains unexplored. The aerodynamic properties of the vehicles, such as drag, lift, stability, wind noise, and the accumulation of water and dirt on the surface of vehicles are result of transient motions of the flow. Understanding of these processes could lead to better design of the aerodynamics and thus improved performance of vehicles. Thus Volvo Car Corporation is working together with Chalmers to develop an unsteady numerical method and to gain a deeper understanding of the unsteady flow around a car.

Shapes of real cars are too complex to be used for detailed flow studies in experiments and numerical simulations. Although these shapes are used in the automotive industry to determine global quantities such as drag or lift, they are not amenable to learning about the interaction of the flow features around the car responsible for its aerodynamic properties. Therefore engineers often study simplified car-like shapes, [2–5], that can produce flow similar to that around a real car.

Most studies of these flows were made only in the wake region and it was found that the wake consists of a near wake (separation bubble) and a pair of counterrotating longitudinal vortices. These longitudinal vortices were first visualized by Ahmed [6], who studied the wake structures behind three vehicle shapes with different rear-end geometries. Bearman et al. [2] studied time-averaged flow structures in the flow behind a simplified vehicle body shape and found that the longitudinal vortices are important features of the vehicle wakes. The same body was used in the study of the influence of the moving floor on aerodynamic forces and the near-wake flow, [7].

A near-wake region behind Ahmed's body, [3], with variable base slant angle (the angle between the roof and the rear face) was studied by Ahmed et al. [3]. They found that the time-averaged wake consists of a pair of horseshoe vortices, situated one above another in the separation bubble, and of trailing vortices coming off the slant side edges. Han [8] used Reynolds-averaged Navier-Stokes equations (RANS) to simulate the flow around the body from [3] and reported that the flow structures are in agreement with those found in experiments, [3]. The computed pressure at the rear vertical face of the body was (for a base slant angle smaller than 20°) underpredicted, resulting in the computed drag being 30% higher than the measured drag, [1,8]. He also found that a flow at the slant angle of the body larger than 30° becomes highly unsteady and cannot be predicted using steady-state RANS simulations.

Duell and George [5,9] made measurements in the wake of a bus-like body based on Ahmed's body, [3], with a rear slant angle of 90°. They reported two periodic processes in the wake corresponding to the dimensionless frequencies at Strouhal numbers 0.069 and 1.16. The lower value was attributed to the periodic interaction of the upper and lower partitions of the ring vortex in the near wake. The higher value was found to be associated to the vortex shedding process in the shear layer. The flow around a similar body was measured by Barlow et al. [4,10] who studied the influence of the aspect ratio (model width/model height) on the aerodynamic forces.

Bearman [11] presented velocity measurements of the wake of a car model. Although he reported a pair of time-averaged counterrotating vortices similar to those found in [6] and [2], he showed that these vortices are formed by a substantial number of instantaneous vortex structures that move randomly in time and space. He thus raised the question of whether the wake flow behind a car can be accurately simulated using RANS equations.

Some early attempts to use transient simulations for this kind of flow are presented in [12–14]. Although the authors of these papers denoted their simulations direct numerical simulations (DNS), [12,13], or large-eddy simulation (LES), [14], we would classify these simulations as very unresolved LES and thus the accuracy of predicted flows is doubtful.

This paper aims to present a LES of the flow studied in [9] and [5]. Being a three-dimensional time-dependent technique, LES should be better suited for this unsteady flow than RANS. It has already been applied to various bluff body flows, [15–17] where it proved to be successful. Our intention is to gain a good understanding of the instantaneous and time-averaged flows around this body. This paper presents not only the drag and lift coefficients that describe the aerodynamic properties of the body, but also the flow structures responsible for these properties.

The paper is organized as follows. Section 2 presents the LES equations and the model representing the influence of the small turbulence scales on the large resolved ones. The numerical method used in this work is summarized in Section 3. Section 4 describes the body, the computational domain, and the boundary conditions used in the simulations and compares them with the ones used in the experiment, [9,5]. Section 5.1 presents the time-averaged and instantaneous flow around the body that resulted

Contributed by the Fluids Engineering Division for publication in the JOURNAL OF FLUIDS ENGINEERING. Manuscript received by the Fluids Engineering Division April 9, 2002; revised manuscript received October 30, 2002. Associate Editor: J. Marshall.

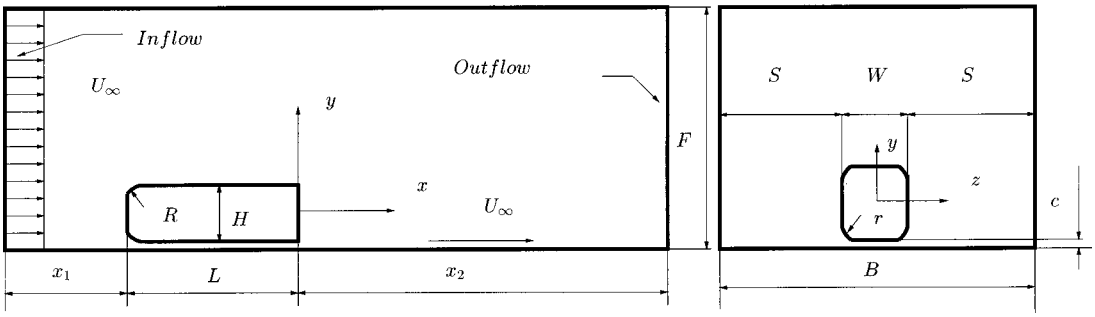

Fig. 1 Geometry of the vehicle body and computational domain

from the simulations and compares them with previous knowledge of this flow. The influence of the flow on the body through the aerodynamic forces is considered in Section 5.2. Section 5.3 presents a comparison of the velocity field in the near wake from the simulations with the one from hot-wire measurements [5,9]. The numerical accuracy is discussed in Section 6. Finally, some concluding remarks are made in Section 7 and some problems with the simulations are discussed.

2 Governing Equations and Subgrid-Scale Modeling

The governing large-eddy simulation (LES) equations are the filtered incompressible Navier-Stokes and the continuity equations filtered with the spatial filter of characteristic width Δ (Δ is the grid resolution in this work):

$$\frac{\partial \overline{u_i}}{\partial t}+\frac{\partial}{\partial x_j}(\overline{u_i}\overline{u_j})=-\frac{1}{\rho}\frac{\partial \overline{p}}{\partial x_i}+\nu\frac{\partial^2 \overline{u_i}}{\partial x_j \partial x_j}-\frac{\partial \tau_{ij}}{\partial x_j} \tag{1}$$

and

$$\frac{\partial \overline{u_i}}{\partial x_i}=0. \tag{2}$$

Here, $\overline{u_i}$ and $\overline{p_i}$ are the resolved velocity and pressure, respectively, and the bar over the variable denotes filtering.

These equations are derived applying a filtering operation

$$\overline{f}(x_i)=\int_\Omega f(x_i')G(x_i,x_i')dx_i' \tag{3}$$

on the Navier-Stokes and the continuity equations, [18]. Here G is a top hat filter function and Ω represents the entire flow domain. The filtered variables in the governing Eqs. (1) and (2) are obtained implicitly through the spatial discretization.

The derivation of Eqs. (1) and (2) from the Navier-Stokes equations, the continuity equation and Eq. (3) requires that the differentiation operations commute with the filtering operator, i.e.,

$$\frac{\overline{\partial f}}{\partial x_i}=\frac{\partial \overline{f}}{\partial x_i}. \tag{4}$$

The commutation property in Eq. (4) is valid if the filter width Δ is constant. However, a variable filter width is used in inhomogeneous flow (including the flow studied in this paper). That results in a violation of Eq. (4). An analysis of the commutation error, [19], shows that the error is of order $\mathcal{O}(\Delta^2)$, and it is thus in this work of the same order as the discretization error.

The goal of the filtering is to decompose the fluid motion into a large-scale component that can be computed exactly and the small subgrid scale (SGS). The influence of the small scales of the turbulence on the large energy carrying scales in Eq. (1) appears in the SGS stress tensor, $\tau_{ij}=\overline{u_iu_j}-\overline{u_i}\overline{u_j}$, which must be modeled. A large number of models for the SGS stress tensor have been proposed in the past four decades (see [20] for a review), most of them built on the algebraic eddy viscosity model originally proposed by Smagorinsky [21]. Although the original Smagorinsky model has some drawbacks, [20], it is used in this paper for its simplicity and low computational cost. The Smagorinsky model represents the anisotropic part of the SGS stress tensor, τ_{ij}, as

$$\tau_{ij}-\frac{1}{3}\delta_{ij}\tau_{kk}=-2\nu_{\text{sgs}}\overline{S}_{ij} \tag{5}$$

where $\nu_{\text{sgs}}=(C_s\Delta)^2|\overline{S}|$ is the SGS viscosity,

$$\overline{S}_{ij}=\frac{1}{2}\left(\frac{\partial \overline{u_i}}{\partial x_j}+\frac{\partial \overline{u_j}}{\partial x_i}\right) \tag{6}$$

is the resolved rate-of-strain tensor and $|\overline{S}|=(2\overline{S}_{ij}\overline{S}_{ij})^{1/2}$. The Smagorinsky constant, C_s, must be adjusted for different flows. The value of $C_s=0.1$ previously used for bluff-body flows, [15–17], is used in this work. This value of C_s is inappropriate in the laminar shear flows since the SGS stresses are zero here, and thus the Smagorinsky coefficient of $C_s=0$ should be used in this region, [22]. The formation of a turbulent boundary layer in the experiment was ensured with boundary layer trip wires mounted at the front of the model. Because of this there is no laminar boundary layer on the body and the assumption of nonzero SGS stresses (i.e., $C_s=0.1$) used in our LES is thus correct. The filter width, Δ, is defined in this work as $\Delta=(\Delta_1\Delta_2\Delta_3)^{1/3}$, where Δ_i are the computational cell sizes in three coordinate directions.

3 Numerical Method

Large-eddy simulation (LES) Eqs. (1) and (2) are discretized using a three-dimensional finite volume method for solving the incompressible Navier-Stokes equations using a collocated grid arrangement, [23]. Both convective and viscous plus subgrid fluxes are approximated by central differences of second-order accuracy. The time integration is done using the Crank-Nicolson second-order scheme. The SIMPLEC algorithm is used for the pressure-velocity coupling. The code is parallelized using block decomposition and the PVM and MPI message passing systems, [24]. Additional details on this code can be found in [23] and [24].

4 Description of the Test Case and Numerical Details

A flow around a bus-shaped body studied in [9] and [5] was computed. The geometry of the computational domain is given in Fig. 1. All the geometric quantities are normalized with the body height, H, equal to 0.125 m. A domain with an upstream length of $x_1/H=8$, a downstream length of $x_2/H=21$, and a spanwise width of $B=5.92H$ was used for the simulation. Similar values for upstream and downstream lengths were found sufficient by Sohankar et al. [25] in large-eddy simulations (LES) of the flow around a square cylinder. Although experimental studies, [5,9], were carried out for several different aspect ratios (W/H), we chose $W/H=1$, for which the drag and lift data exist from another experiment, [4,10] using a similar body. The values of the other geometrical quantities are $L/H=3.68$, $S/H=2.46$, $R/H=0.152$,

$r/H=0.1016$, and $F/H=4$. As can be seen from the radii R/H and r/H the roundness of this model is exaggerated compared to full-scale bus. This is common practice in the experimental studies of reduced scale models, [1]. The ground clearance of $c/H=0.08$ is similar to the clearance ratio of buses. The Reynolds number $\mathrm{Re}=U_\infty H/\nu$ was 0.21×10^6. As it will be shown later in the paper, the choice of such a low Reynolds number (low from vehicle aerodynamics perspective) will have some implications on the flow around the fore-body of the bus but the LES of the higher Reynolds number flow was not feasible at the time of this work.

In the experimental setup, the location of the front side relative to the inlet was $4.512H$ and the distance from the test section exit to the back wall perpendicular to the flow was $14.832H$. A moving ground belt and boundary layer scoop were used to simulate the floor boundary condition and to minimize boundary layer effects. The cross section of the tunnel test section, the ground clearance, and the position of the model's cross section with respect to the tunnel were identical in LES and the experimental setup.

In the experiments of Duell and George [5,9], the inlet mean velocity was uniform within 1% and the average turbulent intensity was 0.3%. A uniform velocity profile constant in time was thus used as the inlet boundary condition in this work. The convective boundary condition $\partial\overline{u}_i/\partial t+U_c\,(\partial\overline{u}_i/\partial x)=0$ was used at the downstream boundary. Here, U_c was set equal to the incoming mean velocity, U_∞. To simulate the moving ground, the velocity of the lower wall was set equal to U_∞. The lateral surfaces were treated as slip surfaces using symmetry conditions, $\partial\overline{u}/\partial z=\partial\overline{v}/\partial z=\overline{w}=0$. No-slip boundary conditions were used on the wall in fine and medium-grid simulations, while the wall functions based on the ''instantaneous logarithmic law'' are used in the coarse-grid simulation. The implementation of the wall functions in the coarse-grid simulation is as follows: The instantaneous logarithmic law of the form

$$\overline{u}^+=\frac{\ln y^+}{0.4}+5.2 \tag{7}$$

is used in the logarithmic region ($y^+\geqslant11.63$ where $y^+=y\overline{u}_\tau/\nu$). Here, $\overline{u}^+=\overline{u}/\overline{u}_\tau$ and the friction velocity is defined as $\overline{u}_\tau=(\tau_{\mathrm{wall}}/\rho)^{1/2}$. Point $y^+=11.63$ is defined as the intersection point between the near wall linear law and the logarithmic law. The linear law ($y^+\leqslant11.63$) is of the form

$$\overline{u}^+=y^+. \tag{8}$$

The approximate boundary condition when $y^+\geqslant11.63$ is implemented in the code by adding the artificial viscosity, ν_{bc}, resulting from the approximate wall boundary condition (7) to the laminar viscosity on the wall. The friction velocity, $\overline{u}_\tau$, is first computed from (7). The wall shear stress is then modeled as

$$\tau_{\mathrm{wall}}/\rho\equiv\left(\nu\frac{\partial\overline{u}}{\partial y}\right)_{\mathrm{wall}}=\nu_{bc}\frac{\overline{u}}{y} \tag{9}$$

where τ_{wall} is the wall shear stress. The artificial viscosity is now determined from the definition of the friction velocity and Eq. (9) as

$$\nu_{bc}=\frac{\overline{u}_\tau^2 y}{\overline{u}}=\frac{\overline{u}_\tau y}{\overline{u}^+} \tag{10}$$

where $\overline{u}^+$ is obtained from (7). The homogeneous Neumann condition was used for the pressure at all boundaries.

To investigate the influence of the near-wall resolution on the results and to establish the results' grid independence, we made computations on three different computational grids. The topology of the grid consists of 24 (coarse and medium grids) and 40 (fine grid) blocks where 6 (coarse and medium grids) and 18 (fine grid) blocks form an *O* grid. An additional larger bus surface was made for the outer surface of the *O* grid. The *O* grid, with a thickness of $0.04H$, was created between this surface and the surface of the vehicle body (see Fig. 2). The total number of cells was 1.8, 2.1, and 4.5 million in the coarse, medium, and fine grids, respectively, resulting in the resolution presented in Table 1.

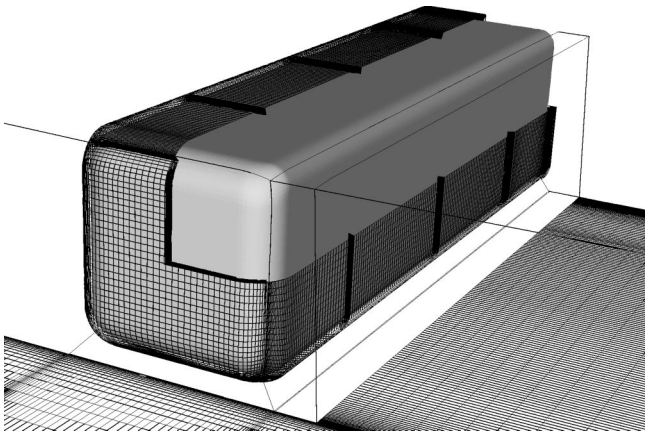

Fig. 2 The topology of the fine grid. Note that only *O* grid and few blocks around it are shown. One-fourth of the *O* grid is removed in this figure.

The time step was 2×10^{-4} in the coarse-grid simulation and 1×10^{-4} in the medium and fine-grid simulations, giving a maximal CFL number of approximately 6.5. The CFL number was smaller than one in 98% of the cells during the entire simulation. The averaging time, tU_∞/H, in the simulation was 94.4 (59,000 time steps), 48 (60,000 time steps), and 62.4 (78,000 time steps) in the coarse, medium, and fine-grid simulations, respectively. The time-averaged streamlines projected onto plane $y=0$ downstream the bus were found to be approximately symmetric with respect to the plane $z=0$ (not shown in the paper) which indicates that the number of averaging samples and the averaging times were sufficient.

5 Results and Discussion

5.1 Description of the Flow. As we will see in this section, the instantaneous coherent structures distinguish themselves from the time-averaged ones. Following the flow along and behind the body, we present these differences below and also fill in the information on the vortices that were not observed in the experiments. All results presented in this section are from the fine-grid computation unless otherwise stated.

Front-End Flow. Although the body has rounded leading edges, the flow separates at the front lateral and roof edges of the body (Figs. 3 and 4). The character of the leading-edge flow (i.e., attached or detached) is dependent of the leading-edge radii and the Reynolds number, [26]. As the Reynolds number is decreased, a more rounded leading edge is needed to avoid separation. The influence of the Reynolds number on the optimum radius (radius that eliminates the flow separation at the front edges) for the edge of a cubic bodies is discussed in [27] and [26]. For example,

Table 1 Spatial resolution expressed in the wall units (e.g., $\Delta s^+=\Delta s\overline{u}_\tau/\nu$, where $\overline{u}_\tau$ is the friction velocity). *s* is the streamwise direction, *n* is the wall-normal direction, and *l* is the direction parallel with the surface of the body and normal to the streamwise direction. Values in parentheses are for the separation bubbles close to the front end. $\langle.\rangle_t$ denotes time averaging.

Case	$\langle\Delta s^+\rangle_t$	$\langle\Delta n^+\rangle_t$	$\langle\Delta l^+\rangle_t$
Coarse	15–580	11.8–18.8	14–217
Medium	15–580 (30–500)	0.8–1.2 (0.5)	14–217 (21–224)
Fine	5–164 (44–153)	0.5–0.8 (0.3)	14–142 (21–100)

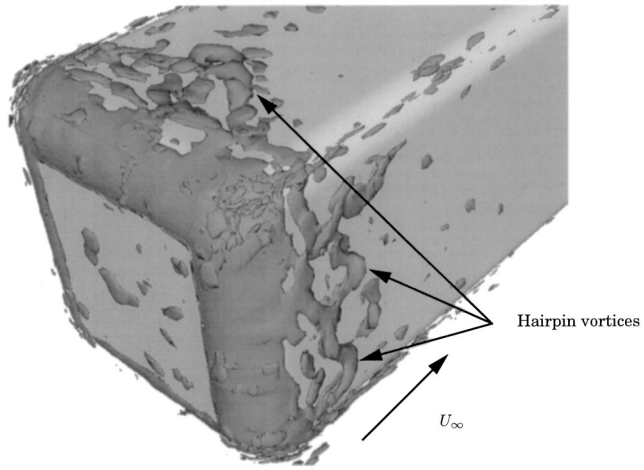

Fig. 3 The isosurface of the instantaneous second invariant of the velocity gradient, [35], $Q=11000$

Hucho et al. [27] found that these radii for $\mathrm{Re}<10^6$ must be $r/H>0.17$, [27], and applying Cooper's, [26], study to the present geometry, with $R/H=0.152$ and $r/H=0.102$, leads to $\mathrm{Re}>0.8\times10^6$ and $\mathrm{Re}>1.3\times10^6$, respectively, to avoid the separation. We thus conclude that the separated flow on the leading edge observed in our simulation is accurately predicted and in agreement with previous knowledge.

The contribution of the fore-body pressure drag to total drag of trucks and buses is small but the generation of the separation regions with recirculating flow close to the leading edges influences the wind generated noise and the accumulation of water and dirt on the surface of vehicle. Therefore the extrapolation of the results from the low-Reynolds study in this paper to high Reynolds number vehicles on the road is of interest. Unfortunately this is not a trivial task owing to the variation in the level of roundedness of the fore-body and the operating Reynolds number. For example for a city bus at operating Reynolds number of 2.2×10^6 (speed of 40 km/h and height of $H=3$ meters), the leading edge radii must be larger than 0.15 meter ($r/H=0.05$, [26]) to avoid separation. The radii on city buses are smaller than this value and the flow after the leading edges is probably detached. On the other hand there are busses and trucks operating on the highway where the fore-body is formed to maintain attached flow. We argue that although the flow is detached on leading edges of the vehicles at lower Reynolds number, the flow is probably attached (if the leading-edge radii are large enough) at higher Reynolds numbers when the aerodynamics is of greater importance. For additional details on the influence of the fore-body radii and the Reynolds number on the flow after leading edges, we refer the reader to [27] and [26].

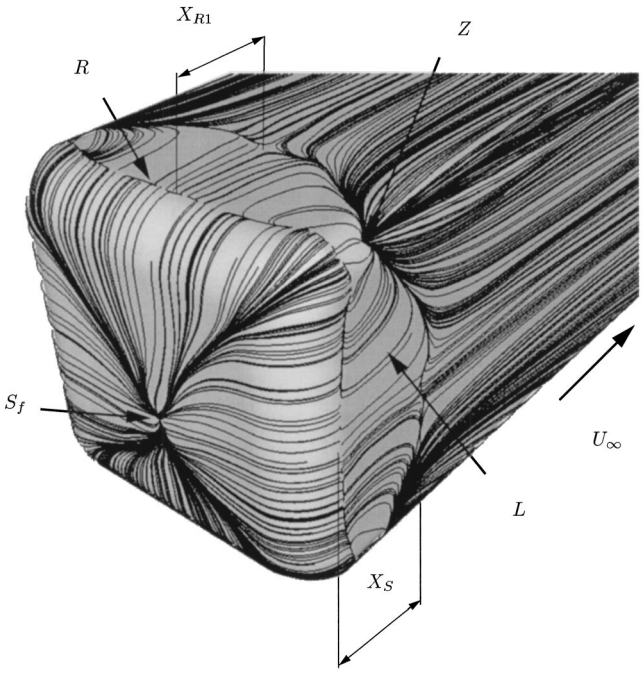

Fig. 4 Time-averaged trace lines on the surface of the body showing the roof vortex, *R*, the lateral vortex, *L*, and the stagnation point, S_f. View of the front face of the body.

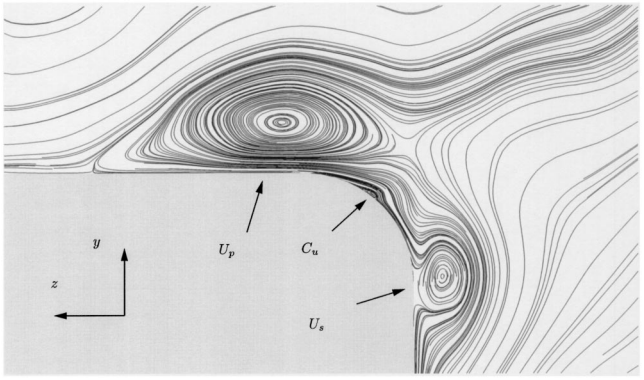

Fig. 5 Time-averaged streamlines projected onto plane $x=-0.8H$. The rotation of U_p and U_s is counterclockwise and clockwise, respectively. View from behind of the upper-right edge of the body.

Vortices parallel with the line of separation are formed in the separation region and transported downstream. They are lifted further back, forming hairpin vortices attached with their two legs to the surface of the body (Fig. 3). They break down shortly after their birth, indicating the reattachment to the body. When time-averaged, they form lateral vortices, L (one on each side of the body), and one vortex on the roof of the body, R (Fig. 4). The positions of these vortices are visualized in Fig. 4, and the reattachment lengths of the lateral vortices and the roof vortex, X_{R1} and X_S, respectively, (Fig. 4) are presented in Table 2. The stagnation point, S_f, located at $y=-0.13H$, $-0.10H$, and $-0.10H$ in the coarse, medium, and fine-grid simulations is shown in Fig. 4.

Trailing Vortices. Close to the upper lateral edges, we find four trailing vortices (two on each side of the bus). Figure 5 shows these vortices for one side of the bus. It can be seen that there is one vortex on each side of the edge (U_p and U_s) and one very thin separation bubble in the middle (C_u). These vortices originate at approximately point Z in Fig. 4 and exist along the entire bus. Their foci have approximately same position in the $y-z$ plane along the body (see [28]).

Similar to the trailing vortices at the upper lateral edges, a pair of trailing vortices is formed around each lower lateral edge of the bus. The size of the vortices on the underbody side is diminished by the small ground clearance, and they are much smaller than those on the lateral side of the edge (T vortices in Fig. 6). These vortices are very thin and are visible only after a very long averaging time as a result of the three-dimensional and unsteady flow underneath the body.

Here we concentrate on the strong trailing vortices on the lateral side of the lower edge of the body (Fig. 6). The right (shown in Fig. 6) and the left vortices rotate counterclockwise and clockwise, respectively. These vortices are present from the reattach-

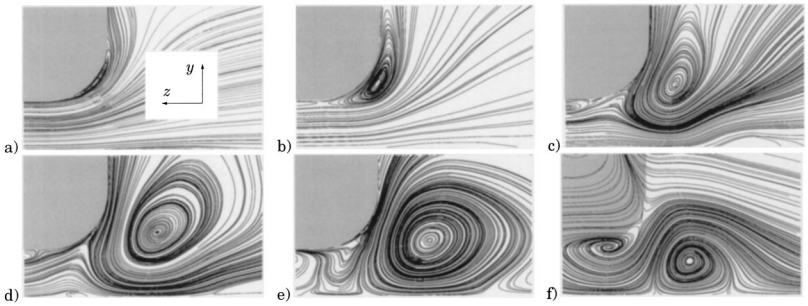

Fig. 6 Time-averaged streamlines projected onto planes: (*a*) $x=-3.36H$, (*b*) $x=-2.88H$, (*c*) $x=-1.68H$, (*d*) $x=-0.48H$, (*e*) $x=0$, and (*f*) $x=0.32H$. The direction of the rotation of this vortex (*T*) is counterclockwise. View from behind of the lower-right edge of the body.

ment of the lateral vortices, *L* (Fig. 4), at $x=-3.36H$ to approximately $x=0.4H$. They are much stronger than the vortices at the upper edges of the body. On their way downstream the *T* vortices first grow in diameter, reaching their maximum in the vicinity of the rear face of the body ($x=0$), and then shrink further downstream (Fig. 6). Although they form at the surface near the reattachment line, they move away from the body in the lateral direction and towards the channel floor as they pass the body (Fig. 6). This motion of the vortices can be explained with their direction of the rotation shown in Fig. 7 and according to reasoning similar to that in potential theory. As they are formed very close to the body surface, they move towards the channel floor in a way similar to the potential vortex and its image replacing the body. Close to the floor, the vortex image in the floor takes over resulting in a sideward deflection. Han [8] found these vortices near the lower lateral edges of the Ahmed's body and concluded that they were formed due to the viscous interaction between the body and the ground-plane boundary layer.

The trailing vortices found in the time-averaged field (Fig. 6) are no longer present in the instantaneous velocity field (Fig. 8). The instantaneous flow is composed of a number of vortex structures that move randomly in time and space (Fig. 8).

Flow Underneath a Bus. It is well known that the flow underneath a passenger car has a three-dimensional character, [1], similar to what is valid for our simplified bus, see Fig. 7. Although the boundary layer is not formed on the moving floor, it is formed along the underbody of the bus. The boundary layer retards the fluid in the streamwise direction and, to satisfy continuity, fluid must either spread outwards to lateral sides or accelerate in the lower part of the channel, and it takes less energy to do the former. This outward motion forms the trailing vortices, *T*, which pump out the fluid from the flow underneath. At the same time, there is a thin region close to the underbody of the bus (see Fig. 7) where the flow moves towards the center plane of the body ($z=0$).

Near-Wake Region With Separation Bubble. The flow separates on the rear edges of the body and forms four secondary vortices, *B* (top, bottom and one on each side, see Figs. 9 and 10), each with its axes parallel to its separation edge. Velocities near the rear edge of the bus are small and difficult to measure, and these structures were therefore not observed in the experiments. Our simulations show that these vortices are very unsteady and thus cannot be studied in RANS simulations, [8]. These vortices have approximately the same size except for the one close to the underbody edge, which is much thinner than the other three vortices. Figure 9 shows that the fine and the medium simulations

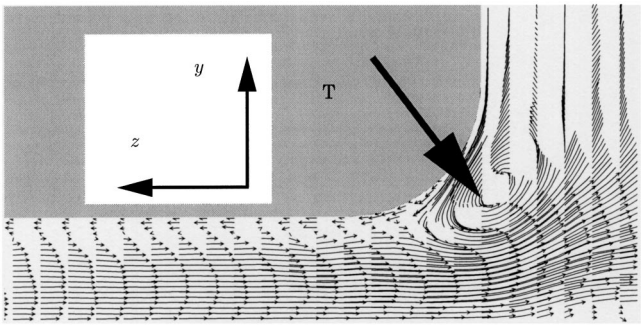

Fig. 7 Time-averaged velocity vectors in plane $x=-1.68H$. View from behind of the lower-right edge of the bus.

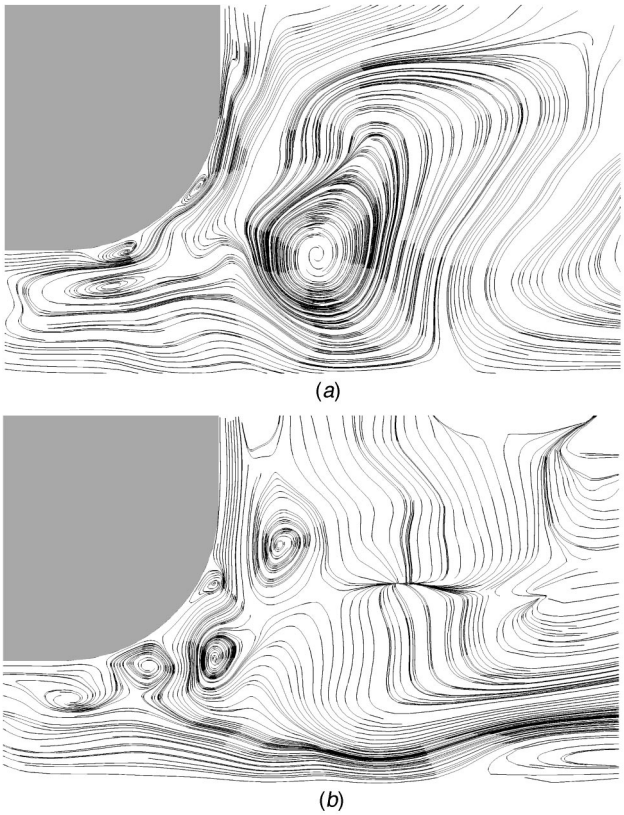

Fig. 8 Instantaneous streamlines at $x=-0.48H$. The time difference between two pictures is $tU_\infty/H=3.2$. View from behind of the lower-right edge of the bus.

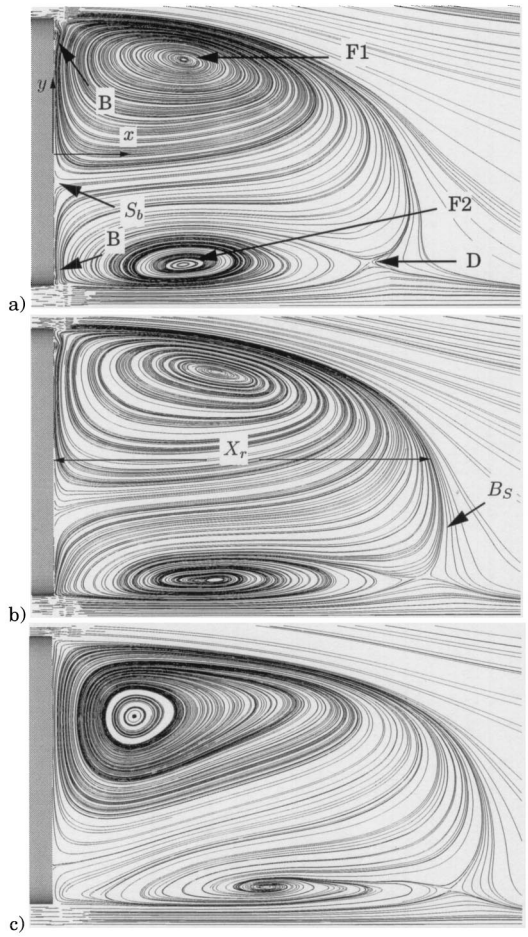

Fig. 9 Time-averaged streamlines projected onto symmetry plane $z=0$ of the bus. (*a*) Fine grid, (*b*) medium grid, (*c*) coarse grid.

predicted these vortices and that the coarse simulation failed to predict them. Two larger counterrotating vortices with foci $F1$ and $F2$ roll up and form a separation bubble (Fig. 9). Although all simulations show these two vortices, there are evident differences in their size and position in the three simulations (Fig. 9).

The first impression in Fig. 9 is that the resolution of the boundary layer on the body is directly responsible for the size of the wake. The free stagnation point (B_s) downstream of the separation bubble is found to be below the center of the rear face of the model, i.e., below $y=0$ (Fig. 9 and Table 2). In the experiments, [5,9], the free stagnation point was assumed to be at $y=0$, where the recirculation length X_r (Fig. 9) was measured. A comparison of this length from our LES with the experimental value is shown in Table 2. Only the fine grid simulation predicted this length close to the experimental value of $1.1H$, and we conclude that the spanwise and streamwise resolution is important for capturing the correct size of the wake.

In agreement with the experiments [5,9] the lower vortex with focus $F2$ is smaller than the upper one (focus $F1$). This is a consequence of the small ground clearance, which reduces the amount of fluid entering the lower vortex. The lower vortex is very unsteady and is averaged from a number of instantaneous vortices (Fig. 11) whereas the upper vortex is also present, slightly modified, in the instantaneous flow. The lower vortex contains approximately the same amount of fluid in the three simulations but the shape is changed (Fig. 9) and the extension of the vortex in x and y directions is decreased and increased, respectively, with the grid refinement. The position of the stagnation point, S_b (Fig. 9), on the rear of the body moves in the positive y-direction while the position of the saddle point, D, moves towards the body with the grid refinement.

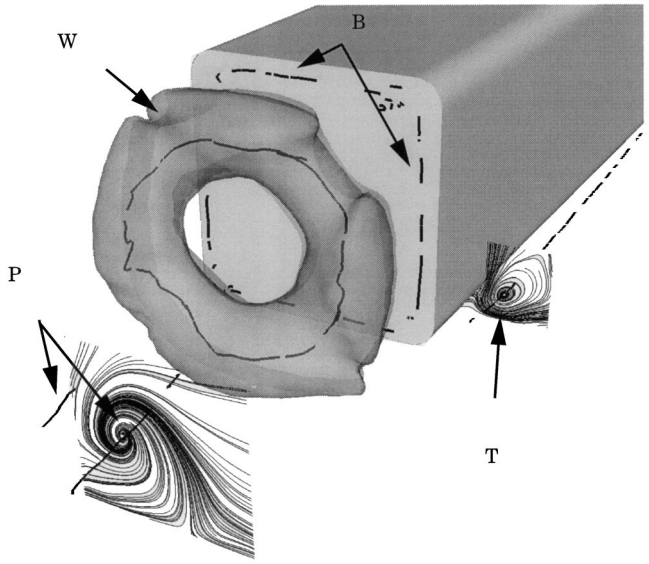

Fig. 10 The isosurface of time-averaged pressure $p=-0.20$. The black curves represent the vortex cores of the thin edge vortices *B*, the ring vortex *W*, and the longitudinal vortices behind the separation bubble *P*. Vortices on the right side ($z<0$), *P* and *T*, are visualized using streamlines in planes $x=1.4H$ and $x=-0.48H$, respectively (note that the mirror image vortices on the left side, i.e., $z>0$, are not shown in this figure). View of the rear face of the body.

Another pair of vortices is formed in the $x-z$ plane, in agreement with results in [9] and [5], and these together with the vortices in the $x-y$ plane form a ring vortex, W (Fig. 10). The cores of ring vortex W, edge vortices B, trailing vortex T, and longitudinal vortices P are visualized in this figure using the critical point theory, [29,30], i.e., we plotted the points whose rate-of-deformation tensor has one real and a pair of complex-conjugate eigenvalues and whose velocity is zero. The formation of a ring vortex was also observed in the experimental study of Ahmed's body but only when the strength of upper and lower horseshoe vortices in the separation bubble was approximately equal, [3]. According to Ahmed [3], the equal strength of these vortices can lead to a merging process of the upper and lower vortices, resulting in a ring vortex. Han [8] confirmed the existence of this coherent structure in the near wake of Ahmed's body, and Duell and George [5,9] found this structure in the near wake of the body. The ring vortex was time-averaged from the instantaneous coherent structure, W_i, shown in Fig. 11. This structure moves back and forth, and its weak periodic pumping motion is correlated with the shedding of the vortices from the end of the separation bubble (Fig. 11). A similar flow structure was found in the experiments [5,9].

Table 2 Lengths for reattachment on the roof (X_{R1}), lateral walls (X_S) and behind the bus (X_r). X_{free} and Y_{free} are coordinates of the free stagnation bubble.

Contribution	X_{R1}/H	X_S/H	X_r/H	X_{free}/H	Y_{free}/H
Duell and George [5]	-	-	1.1	-	-
Coarse	0	0	1.44	1.6	−0.17
Medium	0.41	0.41	1.42	1.42	−0.23
Fine	0.33	0.33	1.18	1.3	−0.2

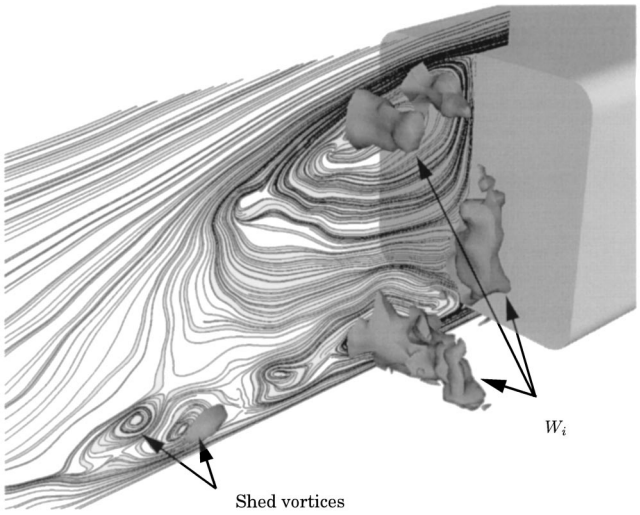

Fig. 11 The instantaneous streamlines projected onto symmetry plane $z=0$ of the bus and the isosurface of the instantaneous pressure, $p=-0.20$. Note that only half of the pressure surface (for $z\leq 0$) is shown.

Longitudinal Vortices Behind the Separation Bubble. The main flow in the streamwise direction interacts with the separation bubble in the wake, resulting in the transverse (i.e., in the y and z-directions) flow. The transverse flow restricts the length of the bubble in the wake and forms a pair of counterrotating longitudinal vortices after the bubble closure (see Fig. 12). One of these vortices ($z<0$) is shown in the plane close to the bubble closure in Fig. 10. Similar vortices were found in the study of the wake structures of different vehicle shapes in [3,4,6] and behind a car model in [11]. The rotation of these vortices is in an inward direction (Fig. 12), transporting the fluid in the space between vortices towards the floor (Fig. 12). This is in agreement with the direction of rotation of vortices in the far wake of a similar body in [4]. The position of these vortices lies about $0.1H$ away from the center plane $z=0$ at their origin ($x=1.3H$). As a result of their inward direction of rotation, their position first moves towards the floor and against each other, similar to a pair of counterrotating potential vortices. As the downwards motion of these vortices is slowed by the presence of the floor, their mutual interaction results in their deflection sideways, away from the symmetry plane $z=0$. This is similar to the interaction of the pair of counterrotating potential vortices and their mirror images replacing the floor. They spread outward with increasing distance from the rear of the bus. They extend far downstream and were detected as far as at the outlet ($x=21H$), where their spanwise position is about $0.85H$ away from plane $z=0$. These results are in agreement with the findings in [6]. The instantaneous wake is different from the time-averaged one and contains not only two longitudinal vortices but a larger number of vortices that move randomly in time and space (Fig. 13). This is in agreement with [11].

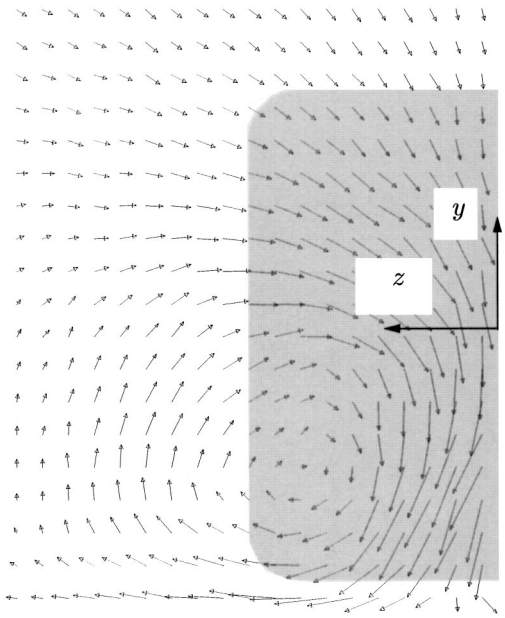

Fig. 12 The time-averaged longitudinal vortex in the far wake in plane $x=3.52H$. View of the rear face of the bus.

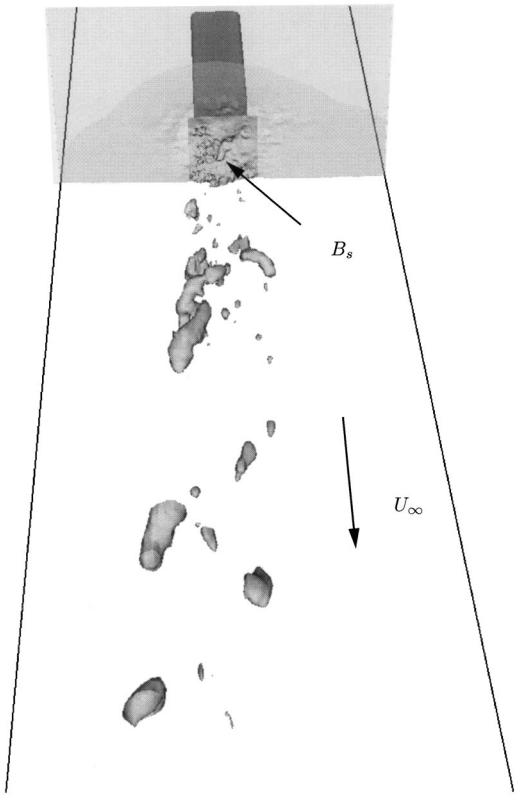

Fig. 13 Instantaneous coherent structures in the far wake visualized with isosurface of pressure $p=-0.035$. B_s is the free stagnation point at the closure of the separation bubble. View of the rear face of the bus.

The time-averaged flow structures around the rear part of the body and in the wake are summarized in the schematic sketch in Fig. 14. One-fourth of the separation bubble is removed in this sketch to show the flow pattern and the direction of the rotation of the vortices. The direction of the rotation of the longitudinal vortices in this figure is indicated with a positive (ω_x^+) or negative (ω_x^-) streamwise vorticity component.

5.2 Aerodynamic Forces. The forces acting on the surface of the body as a result of the surface pressure were studied both time-averaged and instantaneously. The drag $\langle C_D\rangle_t$ and lift $\langle C_L\rangle_t$ coefficients that are interesting in engineering are presented in Table 3. Drag coefficient $\langle C_D\rangle_t=0.33$ in the fine-grid simulation is equal to the value measured for an almost identical body in [10]. The aspect ratio ($AR=W/H$) and the ground clearance for the body in [10] are equal to the ones for the body studied here. Although the Reynolds number was higher in [10] (1.6×10^6

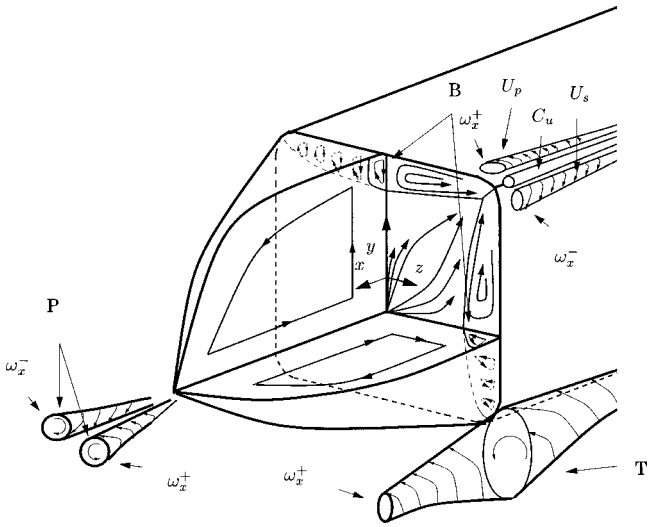

Fig. 14 Schematic representation of the time-averaged wake flow.

based on the body height and incoming velocity), it is probably a good assumption that the wake flow, responsible for the chief part of the total drag, becomes Reynolds-number independent at Re $=0.21\times10^6$. Table 3 shows that 69% of the pressure drag comes from the rear face.

As can be seen in Table 3, the bus is exposed to a negative lift (down force). The values of the time-averaged lift coefficient in Table 3 are close to the value of -0.06 measured in [10].

The r.m.s. values of the drag and lift coefficients were $C_{D_{\text{rms}}}=0.0075$ and $C_{L_{\text{rms}}}=0.0033$, respectively, in the fine-grid simulation. In addition to these design-relevant quantities, we studied the side force coefficient, C_S, and found that it varied with $C_{S_{\text{rms}}}=0.0039$ in the fine-grid simulation. The time history of these coefficients was paid special attention and the coefficient signals were Fourier transformed, resolving their dominating frequencies. Four dominating peaks are found in the Fourier transform of C_D at the Strouhal numbers of $\text{St}=fH/U_\infty=0.061$, 0.14, 0.43, and 0.73 in the fine-grid simulation. The periodic motion containing the most energy is $\text{St}=0.061$, but the reliability of this frequency is weak owing to the short time history (averaging time corresponds to approximately four periods of the signal). There were no peaks in the Fourier transform of C_L, and two main frequencies at $\text{St}=0.22$ and $\text{St}=0.6$ were observed in the side-force signal. The main frequency of the spanwise motion, $\text{St}=0.22$, is close to the shedding frequency of transverse vortices of St $=0.23$ found in Bearman's study of the wake behind a car model, [11]. The similarity of the spanwise motions behind these two different vehicle bodies raises the possibility that a similar vortex shedding exists behind other vehicle bodies.

Unfortunately, only the pressure coefficient $C_p=(p-p_\infty)/(0.5\rho U_\infty^2)$ at the rear face of the body was measured in the experiments of Duell and George [5,9]. The integrated value of C_p over the rear surface, $\langle\overline{C_p}\rangle_t$, measured in the experiment is -0.286 and is lower than the values resulting from our simulations (Table 3). One explanation for the discrepancy between LES and experimental data is that, in our LES, we could not afford to resolve the boundary layer on the lateral walls of the channel, thereby reducing the blockage of the cross section. A simple estimation of the displacement thickness at the position of the rear surface of the body gives a 5% decrease in the dynamic pressure, which is exactly the difference between our LES results and the experimental data.

Table 3 Time-averaged pressure drag, lift, and rear pressure coefficients and dominating frequency (St_p) of the $\overline{C_p}$ signal (note that $\overline{C_p}$ means the integrated C_p over the rear surface)

Case	$\langle C_D\rangle_t$	$\langle C_L\rangle_t$	$\langle\overline{C_p}\rangle_t$	St_p
Coarse	0.206	-0.066	-0.216	0.073
Medium	0.318	-0.066	-0.224	0.055
Fine	0.33	-0.071	-0.229	0.059

The $\overline{C_p}$ signal was also Fourier transformed, revealing a dominating frequency presented in Table 3 that is very close to the frequency of C_D (St$=0.061$) presented above. The characteristic frequency of the $\overline{C_p}$ signal (Table 3) compares well with the experimental value, [5,9] of $\text{St}=0.069$ (note that this value is measured with static and not moving ground, [5]). Baker [31] discussed the characteristic oscillation frequency for a wide range of different ground vehicle bodies and noted that the frequency of $\text{St}=0.05$, which is close to the values in Table 3, is dominant for at least some of these bodies. He concluded that this oscillation can be, as in the case of the bus studied in this paper, due to a pumping of the reverse flow region immediately behind the vehicle (see [5]) or a characteristic frequency of the entire wake.

5.3 Comparison of the Velocities With the Experimental Data. Duell and George [5,9] used hot-wire anemometry for velocity measurements. The near-wake flow is highly turbulent, with regions of reversed flow, and hence velocity measurements cannot be made accurately using single nonpulsed hot wire, [5,7]. Since there are no other velocity data except those in [5], we used these data for comparison with our LES results.

The velocity reported by Duell and George [5,9] was $\overline{V}_{\text{eff}}=(\overline{U}^2+\overline{V}^2)^{1/2}$ where $\overline{U}$ and $\overline{V}$ are the time-averaged velocity components in the x and y-directions, respectively. We computed $\overline{V}_{\text{LES}}=(\langle\overline{u}\rangle_t^2+\langle\overline{v}\rangle_t^2)^{1/2}$ and compared it with their experimental data in Fig. 15. Here, $\langle\overline{u}\rangle_t$ and $\langle\overline{v}\rangle_t$ are the time-averaged resolved velocity components in the x and y-directions, respectively, obtained from LES.

Although the shapes of the computed profiles in the separation bubble ($x/H=0.32$ and $x/H=0.98$) are similar to those of the experiments, there are some differences in the core of the bubble (Fig. 15). The agreement of the experimental data inside the separation bubble with LES results becomes worse with grid refinement (Fig. 15). To explain this behavior we computed the r.m.s. velocity intensity in the separation bubble and found that these were locally higher than 55% of the time-averaged velocity. Duell [5] found that these intensities varied between 32% and 70%. According to Chandrsuda and Brashaw [32], the hot-wire measurements are reliable only if the r.m.s. velocity intensity is less than about 30%. Chandrsuda and Brashaw [32] also found that, when the turbulence intensity exceeds 50%, hot-wire results become highly unreliable. From this we conclude that the experimental data are not accurate in this region. Position $x/H=1.63$ is downstream of the separation bubble, but the local turbulence intensity is still in excess by some 30% of the time-averaged velocity. Figure 15 shows that, at $x/H=1.63$, agreement between computed and measured profiles becomes better with better spatial resolution.

6 Comparison of the Three Simulations

The accuracy of the numerical results in this paper is judged from the grid refinement study. There is a 24% difference in reattachment lengths X_{R1} and X_S between the fine and medium-grid simulations (Table 2). The corresponding difference in the reattachment length, X_r, measured at $y=0$ was 20%, but the difference in the position of the free stagnation point, X_{free}, was only 9%. The value of X_r from the coarse-grid simulation differed by only 1% from the medium-grid value (Table 2). There is a 6% difference in the time-averaged drag coefficient $\langle C_D\rangle_t$ between the fine and the medium-grid simulations and a 54% difference

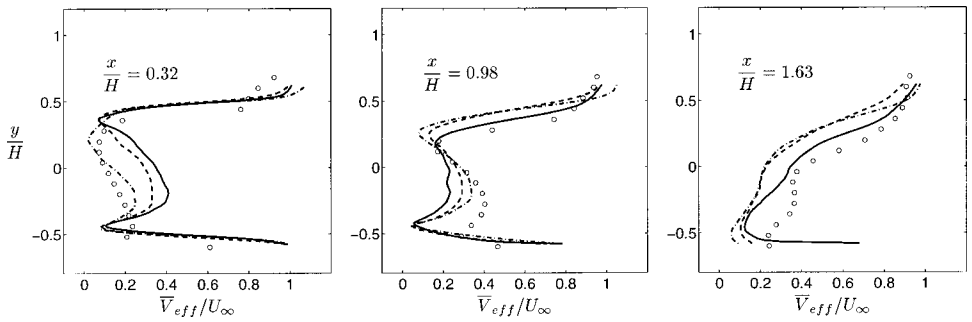

Fig. 15 Time-averaged velocity profiles at three downstream locations at $z=0$. Fine grid (solid curve); medium grid (dashed curve); coarse grid (dashed-dotted curve); experiment (symbols).

between the medium and the coarse-grid simulations (see Table 3). The great difference in $\langle C_D \rangle_t$ between the medium and the coarse-grid simulations is caused by the failure of the coarse-grid simulation to predict separation regions R and L in Fig. 4, thus producing too low a surface pressure at the front edges of the body. The time-averaged lift coefficient $\langle C_L \rangle_t$ remained unchanged between the coarse and medium-grid simulations and decreased by some 6% from the medium to the fine-grid simulations. The time-averaged pressure coefficient at the rear face of the body $\langle C_p \rangle_t$ changed by 3–4% with different spatial resolutions (Table 3). The velocity profiles changed most in the wake region (Fig. 15), but the trend is consistent with grid refinement.

None of the three grids was sufficient for accurate representation of the coherent structures in the boundary layer which are responsible for the maintenance of turbulence. Thus we constructed such a grid with the resolution on the body expressed in the wall units $\langle \Delta s^+ \rangle_t = 30-145$, $\langle \Delta n^+ \rangle_t = 0.5-0.8$ and $\langle \Delta l^+ \rangle_t = 14-35$. Here $\Delta f^+ = \Delta f \overline{u_\tau}/\nu$, $\overline{u_\tau}$ is the friction velocity and $\langle \cdot \rangle_t$ denotes time averaging, s is the streamwise direction, n is the wall-normal direction, and l is the spanwise direction. The resulting structured grid contains 9.8×10^6 cells, of which approximately 2×10^6 cells are located in the near-wall region ($y^+ < 20$). Note that the resolution of the boundary layers on the lateral walls and the ceiling of the wind tunnel was not considered here. If the refinement of the grid was made also on the tunnel walls the size of the grid would be very large. Thus the simulation was not performed on this grid. Additional details on the estimation of the spatial resolution and its extension to the high Reynolds number flow can be found in [33].

7 Concluding Remarks

While the flow around car-like bodies is highly unsteady, our knowledge of this flow is based primarily on experimental and numerical studies of the time-averaged flow. This has been the main obstacle in the development of accurate models for this flow. The large-eddy simulation used in this study predicted not only large-scale coherent structures that agree with previous knowledge but also some new, smaller structures. The latter were either too close to the wall to be observed in experiments or too unsteady to be predicted using RANS simulations. This study has shown that the instantaneous flow is very different from the time-averaged one, not only in the wake but also along the entire body. This suggests revision of the established picture of this flow. The instantaneous coherent structures can either appear randomly in time and space, such as those in the far wake, or in a periodic motion such as those shed from the rear edges. The three-dimensional picture of the flow underneath the body has been confirmed and explained by the growth of the boundary layer on the underbody. It has been shown that the flow near the lower lateral edges is highly unsteady, with a substantial number of instantaneous longitudinal vortices that average to two strong and two weak time-averaged vortices. These instantaneous vortices, together with the lateral vortices, close to the front face of the body, and the longitudinal vortices in the far wake are responsible for the variation of the side force on the body. Prediction of these vortices is thus important for traffic safety and comfort.

Very fine spatial resolution ($\langle \Delta n^+ \rangle_t \leq 1$, $\langle \Delta l^+ \rangle_t = 14$, where n is the wall-normal direction and l is the direction parallel with the surface of the body and normal to the streamwise direction) close to the edges of the body used in two of the simulations resolved two pairs of the time-averaged longitudinal vortices along the upper lateral edges of the body. These were also averaged from a number of unsteady instantaneous vortices.

The existence of the time-averaged vortex ring in the near wake suggested by previous studies, [3,5,8,9], was confirmed, and the pumping frequency of the instantaneous structures was found to be responsible for the periodic variation of the drag on the body.

The resolution of the low-frequency change in the pressure on the rear face of the bus requires very long time-averaging. This together with the costly grid refinement studies needed to prove the numerical accuracy are the main problems to overcome in large-eddy simulations of this kind of flow. These will be solved to some extent by increases in computer power.

The results from this study cannot be directly translated to the high Reynolds number flow owing to possible differences in the region around the fore-body of the bus. Still, we believe that the rest of the flow does not change much with the increase in Reynolds number. We motivate this with findings by Rodi et al. [34]. These authors presented results from the simulations of flow around a surface-mounted cube at two different Reynolds numbers, 3000 and 40,000, based on the incoming velocity and cube height. They found a great similarity in the results for these two flows. Time-averaged coherent structures had almost identical shapes and sizes in the two flows. Thus it seems likely that the qualitative knowledge about the flow around three-dimensional bluff bodies (such as a car) can be extracted from the flow at lower Reynolds number. This observation is not new and has long been used for experimental studies, [2–5]. Note, however, that the choice of the lower Reynolds number, which is high enough to produce a flow similar to that around a full-scale vehicle, is not trivial.

The knowledge gained in this work will hopefully help engineers to understand the flow around similar bodies at higher Reynolds number and to develop better turbulence models for RANS equations.

Acknowledgments

This work was supported by National Swedish Board for Technical Development (NUTEK), the Swedish Agency for Innovation Systems (VINNOVA), and Volvo Car Corporation. Computer time on the SGI ORIGIN 2000 machines, provided by UNICC at Chalmers, is gratefully acknowledged. The authors wish to thank Gunnar Johansson for helpful discussions.

References

[1] Hucho, W-H., 1998, *Aerodynamics of Road Vehicles*, 4th Ed., Society of Automotive Engineers, Warrendale, PA.

[2] Bearman, P. W., Davis, J. P., and Harvey, J. K., 1983, ''Measurement of the Structure of Road Vehicle Wakes,'' *International Journal of Vehicle Design* (Technological Advances in Vehicle Design Series, SP3, Impact of Aerodynamics on Vehicle Design), pp. 493–499.

[3] Ahmed, S. R., Ramm, G., and Faltin, G., 1984, ''Some Salient Features of the Time Averaged Ground Vehicle Wake,'' SAE Paper No. 840300.

[4] Barlow, J., Guterres, R., Ranzenbach, R., and Williams, J., 1999, ''Wake Structures of Rectangular Bodies With Radiused Edges Near a Plane Surface,'' SAE Paper No. 1999-01-0648.

[5] Duell, E. G., and George, A. R., 1999, ''Experimental Study of a Ground Vehicle Body Unsteady Near Wake,'' SAE Paper No. 1999-01-0812.

[6] Ahmed, S. R., 1981, ''Wake Structures of Typical Automobile Shapes,'' ASME J. Fluids Eng., **103**, pp. 162–169.

[7] Bearman, P. W., De Beer, D., Hamidy, E., and Harvey, J. K., 1989, ''The Effect of a Moving Floor on Wind-Tunnel Simulation of Road Vehicles,'' SAE Paper No. 880245.

[8] Han, T., 1989, ''Computational Analysis of Three-Dimensional Turbulent Flow Around a Bluff Body in Ground Proximity,'' AIAA J., **27**(9), pp. 1213–1219.

[9] Duell, E. G., 1994, ''Experimental Investigation of Unsteady Near Wakes of Ground Vehicle Bodies,'' Ph.D. thesis, Cornell University, Ithaca, NY.

[10] Barlow, J. B., Guterres, R., and Ranzenbach, R., 1999, ''Rectangular Bodies With Radiused Edges in Ground Effect,'' AIAA Paper No. 99-3153.

[11] Bearman, P. W., 1997, ''Near Wake Flows Behind Two- and Three-Dimensional Bluff Bodies,'' J. Wind. Eng. Ind. Aerodyn., **69–71**, pp. 33–54.

[12] Kataoka, T., China, H., Nakagawa, K., Yanagimoto, K., and Yoshida, M., 1991, ''Numerical Simulation of Road Vehicle Aerodynamics and Effect of Aerodynamic Devices,'' SAE Paper No. 910597.

[13] Hashiguchi, M., Kawaguchi, K., Yamasake, R., and Kuwahara, K., 1989, ''Computational Study of the Wake Structure of a Simplified Ground-Vehicle Shape With Base Slant,'' SAE Paper No. 890597.

[14] Aoki, K., Ohbayashi, T., Zhu, M., and Miyata, H., 1993, ''Finite-Volume Simulation of 3D Vortical Flow-Fields About Road Vehicles With Various After-Body Configuration,'' SAE Paper No. 931896.

[15] Sohankar, A., Davidson, L., and Norberg, C., 2000, ''Large Eddy Simulation of Flow Past a Square Cylinder: Comparison of Different Subgrid Scale Models,'' ASME J. Fluids Eng., **122**(1), pp. 39–47.

[16] Sohankar, A., Davidson, L., and Norberg, C., 2000, erratum, ASME J. Fluids Eng., **122**(3), p. 643.

[17] Krajnović, S., and Davidson, L., 2002, ''Large Eddy Simulation of the Flow Around a Bluff Body,'' AIAA J., **40**(5), pp. 927–936.

[18] Ghosal, S., 1999, ''Mathematical and Physical Constraint on Large-Eddy Simulations of Turbulence,'' AIAA J., **37**(2), pp. 425–433.

[19] Ghosal, S., and Moin, P., 1995, ''The Basic Equations for the Large Eddy Simulation of Turbulent Flows in Complex Geometry,'' J. Comput. Phys., **118**(1), pp. 24–37.

[20] Meneveau, C., and Katz, J., 2000, ''Scale-Invariance and Turbulence Models for Large-Eddy Simulation,'' Annu. Rev. Fluid Mech., **32**, pp. 1–32.

[21] Smagorinsky, J., 1963, ''General Circulation Experiments With the Primitive Equations,'' Mon. Weather Rev., **91**(3), pp. 99–165.

[22] Pope, S. B., 2000, *Turbulent Flows*, 1st Ed., Cambridge University Press, Cambridge, UK.

[23] Davidson, L., and Farhanieh, B., 1995, ''CALC-BFC: A Finite-Volume Code Employing Collocated Variable Arrangement and Cartesian Velocity Components for Computation of Fluid Flow and Heat Transfer in Complex Three-Dimensional Geometries,'' Report 95/11, Department of Thermo and Fluid Dynamics, Chalmers University of Technology, Gothenburg.

[24] Nilsson, H., and Davidson, L., 1998, ''CALC-PVM: A Parallel SIMPLEC Multiblock Solver for Turbulent Flow in Complex Domains.'' Internal Report 98/12, Department of Thermo and Fluid Dynamics, Chalmers University of Technology, Gothenburg.

[25] Sohankar, A., 1998, ''Numerical Investigation of Vortex Shedding Around Square Cylinders at Low Reynolds Number,'' Ph.D. thesis, Department of Thermo and Fluid Dynamics, Chalmers University of Technology, Gothenburg.

[26] Cooper, K. R., 1985, ''The Effect of Front-Edge Rounding and Rear Edge Shaping on the Aerodynamic Drag of Bluff Vehicles in Ground Proximity,'' SAE Paper No. 850288.

[27] Hucho, W. H., Janssen, L. J., and Emmelmann, H. J., 1976, ''The Optimization of Body Details–A Method for Reducing the Aerodynamic Drag of Road Vehicles,'' SAE Paper No. 760185.

[28] Krajnović, S., and Davidson, L., 2002, ''A Test Case for Large-Eddy Simulation in Vehicle Aerodynamics,'' *Proceedings of the 5th International Symposium on Engineering Turbulence Modelling and Measurements*, W. Rodi and N. Fueyo, eds., Mallorca, Spain, Elsevier, New York, pp. 647–656.

[29] Chong, M. S., Perry, A. E., and Cantwell, B. J., 1990, ''A General Classification of Three-Dimensional Flow Fields,'' Phys. Fluids, **5**(2), pp. 765–777.

[30] Sujudi, D., and Haimes, R., 1995, ''Identification of Swirling Flow in 3-D Vector Fields,'' AIAA Paper No. AIAA 95-1715.

[31] Baker, C. J., 2001, ''Flow and Dispersion in Ground Vehicle Wakes,'' J. Fluids Struct., **15**(7), pp. 1031–1060.

[32] Chandrsuda, C., and Bradshaw, P., 1981, ''Turbulence Structures of Reattaching Mixing Layer,'' J. Fluid Mech., **110**, pp. 171–194.

[33] Krajnović, S., 2002, ''Large Eddy Simulations for Computing the Flow Around Vehicles,'' Ph.D. thesis, Department of Thermo and Fluid Dynamics, Chalmers University of Technology, Gothenburg.

[34] Rodi, W., Ferziger, J. H., Breuer, M., and Pourquié, M., 1997, ''Status of Large-Eddy Simulations: Results of a Workshop,'' ASME J. Fluids Eng., **119**, pp. 248–262.

[35] Jeong, J., and Hussain, F., 1995, ''On the Identification of a Vortex,'' J. Fluid Mech., **285**, pp. 69–94.